Article citation info:
Peng J, Fang B, Li S, Luo J, Zhu X, Ma S. MEMS photoacoustic sensor transformer fault diagnosis method based on gam-mtn. Diagnostyka. 2025;26(2):2025201. https://doi.org/10.29354/diag/202868.



**DIAGNOSTYKA**, 2025, Vol. 26, No. 2

**e-ISSN** 2449-5220
**DOI:** 10.29354/diag/202868

# MEMS PHOTOACOUSTIC SENSOR TRANSFORMER FAULT DIAGNOSIS METHOD BASED ON GAM-MTN

**Jiaqi PENG** *, **Baomin FANG**, **Shou LI**, **Jin LUO**, **Xiaobin ZHU**, **Shunqing MA**

Haidong Power Supply Company, State Grid Qinghai Provincial Electric Power Company, Qinghai 810699, China
* Corresponding author, e-mail: pjq15597275739@163.com

Abstract

As the service life of electrical equipment increases, it may suffer from various faults, such as overheating, partial discharge, etc., resulting in the generation of dissolved gases in the oil. MEMS photoacoustic sensors analyze acoustic signals through photoacoustic spectroscopy and signal processing technology to detect the concentration of dissolved gases in oil. Regarding the data traits of photoacoustic sensors, this document suggests a graph mutual mapping transmission network (GAM-MTN) method. First, an improved aggregation weight graph convolutional neural network is introduced, and the node aggregation weight function is designed using the Manhattan distance metric, so that the model can dynamically adjust the aggregation weight according to the similarity between nodes during the message passing aggregation process. Secondly, the graph mutual mapping transmission network is proposed to achieve uniform spread of origin field and destination field samples through sample mapping technology, which effectively improves the overall migration effect of the model. Finally, unsupervised adaptation of the classifier and domain discriminator is utilized to enhance the generalization capability of the system. Test outcomes demonstrate that the suggested GAM-MTN network can effectively improve the learning efficiency and diagnosis accuracy of transformer fault characteristics. Compared with other advanced neural network models, the recognition accuracy is as high as 96.37%.

Keywords: MEMS photoacoustic sensor; dissolved gas in oil; graph convolutional neural network; chart reciprocal mapping transfer web; defect detection

## 1. INTRODUCTION

In the power system, the transformer is one of the key equipment's, and its stable operation is crucial to the safety and economical functioning of the whole electricity network. However, during long-term operation, the transformer may cause internal faults due to overheating, partial discharge, etc. These issues not only impact the lifespan and efficiency of the transformer itself, but might also jeopardize the safety and reliability of the electricity network. In recent years, with the advancement of power technology, the need for transformer condition monitoring is growing, and dissolved gas analysis in transformer oil, as an effective method, is widely used in early fault detection and diagnosis of transformers.

Recently, profound learning has attained notable outcomes in areas like fault diagnosis [1-4]and industrial analysis [5-8], but it also faces huge challenges. Especially in processing multi-condition and multi-source heterogeneous transformer monitoring data, traditional deep learning models struggle to effectively capture the nonlinear coupling relationships between equipment state features and complex operating conditions. An increasing number of applications require the analysis of non-Euclidean data as graphs or manifolds. Research on how to generalize deep learning algorithms and unsupervised learning methods to graphs has become a hot topic [9-10]. The earliest attempts to generalize neural networks to graphs were Scarselli et al. and Li et al. [11-12]. However, these methods exhibit inherent limitations when handling dynamically evolving equipment state graphs, including rigid node correlation intensity calculations and insufficient adaptability to topological variations. They used a recurrent neural structure to propagate neighboring node information and aggregate it to achieve learning and representation of target nodes. Bruna and Mallat [13] proposed a graph convolutional neural network. Subsequently, Defferrard et al. [14] and others parameterized the convolution kernel in the spectral method, which greatly reduced the spatiotemporal complexity of the graph convolutional neural network model, but it used the local neighborhood information of the node for convolution. operations,

Received 2024-12-17; Accepted 2025-02-11; Available online 2025-02-12

there are limitations on the information utilization capabilities of the global graph structure. This leads to scenarios where critical fault pattern feature responses are easily overwhelmed by local noise in transformers with concurrent multi-fault conditions. However, CNN utilized in profound learning techniques has issues of sluggish convergence and inadequate processing efficiency. To address these deficiencies of CNN, Pang et al. [15] devised a residual CNN grounded on Bayesian optimization for defect detection. Goay et al. [16] suggested a flexible ongoing division method grounded on CNN and extended temporary memory. Zhu et al. [17] describe a CNN-SVM network model. Jin et al. [18] adopt lightweight neural networks for defect detection, thereby reducing system intricacy and education duration. These techniques enhance the alignment speed of CCN. However, there remains potential for enhancement. Particularly in cross-domain migration scenarios, existing methods lack dynamic compensation mechanisms for feature distribution shifts, hindering their adaptability to environmental discrepancies across different substations.

In recent years, research on fault diagnosis using MEMS sensors has made significant progress, providing strong technical support for equipment health management in multiple fields. Lavasani et al. [19] have performed thorough investigation into the application of MEMS sensors in extreme environments. Notably, the synergistic application of MEMS sensor arrays and graph neural networks provides a novel technical pathway for constructing multi-physics-coupled transformer state graphs. By optimizing sensor materials and packaging technology, they have greatly improved the temperature resistance and corrosion resistance of the sensors, and broadened the scope of MEMS sensors. Sensor application scenarios. Kamada et al. and Akita et al. [20-21] and others have explored the integration of MEMS sensors and Internet of Things (IoT) technology, and proposed a fault diagnosis platform based on cloud computing, realizing the entire process from data collection to fault identification. Automation greatly enhances the efficacy and precision of fault diagnosis. Nevertheless, current systems face unresolved challenges in decoupling feature extraction and domain adaptation during real-time data processing, demonstrating suboptimal performance when analyzing dissolved gas-in-oil monitoring data characterized by temporal correlations and spatial diffusivity.

In summary, this paper proposes a graph mutual mapping transmission network (GAM-MTN) method. First, an improved aggregation weight graph convolutional neural network is introduced, and the node aggregation weight function is designed using the Manhattan distance metric, so that the model can dynamically adjust the aggregation weight according to the similarity between nodes during the message passing aggregation process. Secondly, the graph mutual mapping transmission network is proposed to achieve uniform spread of origin field and destination field samples through sample mapping technology, which effectively improves the overall migration effect of the model. Finally, unsupervised adaptation of the classifier and domain discriminator is utilized to enhance the broadening capability of the system.

## 2. GAM-MTN MODEL

### 2.1. Improved graph convolutional neural network model

In order to splice the graph node embedding method based on message passing into a graph convolutional neural network (GCN), a dual-layer chart convoluted neural web model is built. The conceptual illustration of the system is depicted in Figure 1, alternatively determined by formula (1):

$$Z = ReLU(\hat{A}ReLU(\hat{A}XW^{(0)})W^{(1)}) \quad (1)$$

In formula (1): $W^{(0)}$, $W^{(1)}$is the neural network weight matrix (this article uses batch gradient descent to train the neural web weight matrix), $X \in R^{N\times F}$ serves as entry matrix, and $Z \in R^{N\times C}$ is the output matrix obtained after two layers of GCN layers.

The classification result $Y$ can be obtained by inputting the input obtained $Z$ through the graph convolutional neural network into the activation function$Y = softmax(Z)$. The activation function is defined as formula (2):

$$softmax(z_k) = \frac{exp(z_k)}{\sum_{k=1}^{c} exp(z_k)} \quad (2)$$

In formula (2):$z_k$is the value of the kth dimension of the encoded node embedding vector$z$, and C is the dimension of the encoded node embedding vector.

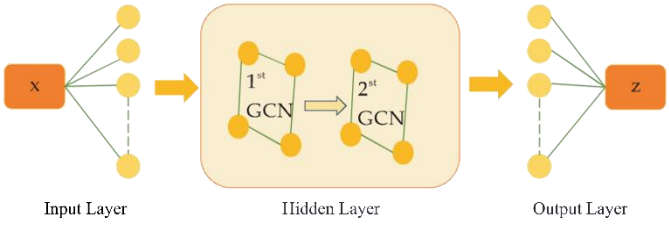


Fig. 1. Schematic Diagram of Graph Convolutional Neural Network Model

Although this model realizes the encoding and generation of graph node embedding vectors, it does not use the characteristics of the nodes themselves in the aggregation process of message transmission, and there are still problems of low information utilization and insufficient aggregation. Therefore, this paper adds a measure of node similarity to change the aggregation weight.

The node similarity is the reciprocal of the distance between nodes, that is, the larger the gap between nodes, the lesser the resemblance. For any two nodes in the graph, there are many ways to measure the distance between them. The classic Minkowski distance measurement function calculation formula is as follows:

$$Dist(x,y) = (\sum_{i=1}^{n} |x_i - y_i|^p)^{\frac{1}{p}} \quad (3)$$

In formula (3): n is the dimension of the node, and p is the hyperparameter. When p=1, it is termed Manhattan span, when p=2, it is named Euclidean span, and when p=∞, it is labeled Chebyshev span. Several distance measurement functions are depicted in Figure 2.

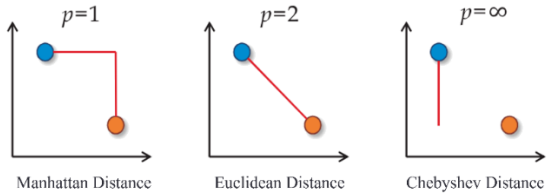


Fig. 2. Schematic Diagram of Distance Metric Functions

This article selects the Manhattan distance when p=1, so that formula (3) is converted into the form of formula (4):

$$Dist(x,y) = \sum_{i=1}^{n} |x_i - y_i| \quad (4)$$

Formula (5) is the graph node embedding formula of the spatial domain graph convolutional neural network, which converts each node in the graph into a vector expressing feature information.

$$h_i^{(l+1)} = \sigma(\sum_{j \in N_i} \theta h_j^{(l)} W^{(l)}) \quad (5)$$

$h_i^{(l+1)}$ represents the attribute array for the point $v_i$ in the (l+1)th tier. $\sigma$ represents a nonlinear activation function, usually using activation functions such as ReLU. $N_i$ represents a node $v_i$; a set of neighbor nodes. where θ is the weight parameter of the message passing aggregation between nodes. $W^{(l)}$ represents the neural network weight matrix of layer l.

Add formula (4) to the node aggregation weight, that is $\theta = \frac{1}{\sqrt{d_i d_j} Dist(h_i,h_j)}$, formula (5) becomes formula (6):

$$h_i^{(l+1)} = \sigma(\sum_{j \in N_i} \frac{1}{\sqrt{d_i d_j} Dist(h_i,h_j)} h_j^{(l)} W^{(l)}) \quad (6)$$

where, $d_i$ denotes the connectivity of the vertex $v_i$ (i.e., the count of links attached to the vertex $v_i$). $d_j$ denotes the connectivity of a vertex $v_j$ (i.e., the count of links attached to the vertex $v_j$). Formula (6) is the improved message passing aggregation function in this article. This function utilizes the architectural details $\sqrt{d_i d_j}$ of the chart and the similarity details $Dist(h_i, h_j)$ between vertex attributes to enhance the precision and alignment rate of the related classification system.

### 2.2. Sample mapping mechanism

Owing to the sluggish alignment rate of convolutional neural network (CNN), an example correspondence method is suggested. Example correspondence techniques employ attribute-based relocation learning to correspond instances in the origin and destination fields to attribute space. Initially, the origin field data processed by the activation mechanism is multiplied by the correspondence coefficient to acquire transformed field data; subsequently, the correspondence coefficient is computed inversely based on the transformed field data; ultimately, the correspondence coefficient is combined with the activated origin field data to attain the corresponded transformed field data. The equivalent procedure is also applied to the destination field data, executing three correspondences. The aim of triadic correspondence is to diminish the variation in attribute spread between fields, augment the impact of example grouping, and boost the efficacy of the entire system. A conceptual illustration of sample mapping is depicted in Figure 3. Suppose that the entry of the origin field is $x = \{x_1, x_2, \dots, x_t\}, x(i) \in R^N, x \in X$, t is the count of operational states, X is the origin field, and N is the count of samples. The entry to the destination field is $y = \{y_1, y_2, \dots, y_t\}, y(i) \in R^N, y \in Y$, Y which is the destination field. The new field space to which the origin field and destination field are corresponded is Z. The outcomes of the initial correspondence of the origin field and destination field $a = \{a_1, a_2, \dots, a_t\}$ and $o = \{o_1, o_2, \dots, o_t\}$ respectively. The outcomes of the secondary correspondence are respectively $b = \{b_1, b_2, \dots, b_t\}$ and $p = \{p_1, p_2, \dots, p_t\}$. The new outcomes corresponded to Z space are respectively $c = \{c_1, c_2, \dots, c_t\}$ and $q = \{q_1, q_2, \dots, q_t\}$. The three correspondence coefficients of the origin field are $A_1$, $A_2$ and $A_3$. The three correspondence coefficients of the destination field are $B_1$, $B_2$ and $B_3$, respectively.

The correspondence equation can be expressed as: $X \times A = Z, Y \times B = Z$ After the origin field and destination field data are processed by the activation mechanism, the correspondence coefficients A and B can represent $A = (X^T X + \lambda I)^{-1} X^T Z$, $B = (Y^T Y + \lambda I)^{-1} Y^T Z$, where λ is the regularization factor. The single correspondence diagram is depicted in Figure 4. The theoretical verification is as outlined below:

Assume the correspondence output is $a = \{a_1, a_2, \dots, a_t\}$, then $a = xA_1$, assuming the matrix $A_h$ represents a weighted graph, there exists a relationship $x = aA_h^T$, Given the local similarity matrix A, the criterion for selecting a good

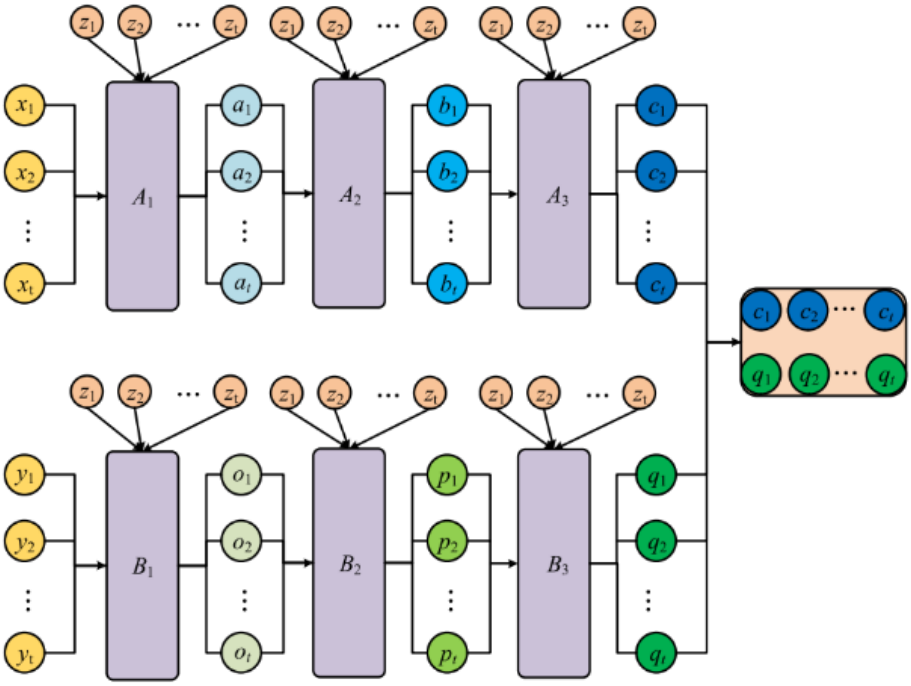


Fig. 3. Sample mapping method

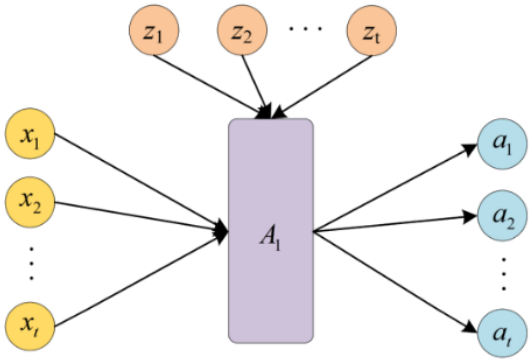


Fig. 4. Single sample mapping method

projection is to minimize the following weighted cost function as shown in Equation (7):

$$\varepsilon(x) = min\left[\frac{1}{2}\sum_{ij} \quad A_{ij}(x_i - x_j)^2\right] \qquad (7)$$

Then we can get formula (8):

$$\varepsilon(x) = Minimize[aA_h^T(D - A)A_h a^T] \qquad (8)$$

To address the issue, apply equality constraints$aDa^T = 1$,$A_h^T aDa^T A_h = 1$ and let L=D-A. Therefore, the minimization problem can be expressed as formula (9):

$$\Omega(Y) = Minimize(aA_h^T LA_h a^T)_{aDa^T=1}(aA_h^T LA_h a^T) \qquad (9)$$

The ideal coefficient A of the restricted goal identified in this study is invertible, and the formula resembles a straight expression. Furthermore, the minimum squares approach employs the squared residual sum to reduce the resolution, rendering the procedure of determining the ideal coefficient A straightforward and efficient. The equation for reducing the squared residual sum is formula (10):

$$Q = min\sum_i \quad (\frac{1}{2}(a_{ie} - a_i)^2) \qquad (10)$$

Among these, $a_{ie}$is the predicted measure, $a_i$is the real measure, and Q is the total of squared differences. Thus, the conversion vector that reduces the target operation $a_i$can be provided through the smallest characteristic value solution of the extended characteristic value issue: $A_h LA_h^T A_h = \lambda A_h DA_h^T$ . Then, the eigenvector $(\lambda_0 \le \lambda_1 \ldots \le \lambda_{G-1})$ and transformation matrix $A_h = (a_0, a_1, \ldots, a_{G-1})$ are defined according to the corresponding eigenvalues. After clustering mapping, the data sample clustering effect is good. Thus, the conversion array$A_h$ is an enhanced mapping. At the same time, the restrictions are: $A_1 A_h a = a$,$A_h A_1 x = x$, which can be obtained: $A_1 A_h = E$, where E is the unit array and $A_1$is the reverse array of$A_h$; these two arrays possess the same correspondence performance. Via the aforementioned verification, the origin field mapping exhibits excellent grouping effect, thereby achieving the attribute enhancement procedure.

### 2.3. Unsupervised adaptation

Exist scarce or no markers in the destination field, thus certain unsupervised field adjustment techniques have been suggested to acquire field consistency and distinctive traits. A conceptual illustration of unsupervised field adjustment is depicted in Figure 5. As depicted in Figure 5, three categories of details play a significant role: class markers, field markers, and data layouts. Class marker details, field marker details, and data layout details are represented by classifiers, field differentiators, and data architectures, individually.

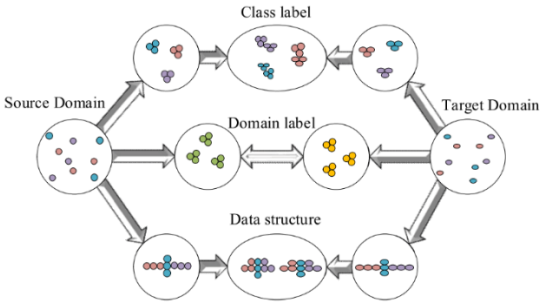


Fig. 5. Unsupervised domain adaptive diagram

It is presumed that the tag spaces of the origin field and the destination field are identical (i.e., Ds = Dt), whereas the attribute spaces As and at are distinct yet interconnected (i.e., input shift). In GAM-MTN, the MMD technique constructs a profound network g: Xt→Dt, capable of forecasting the instance tag of the destination field. MMD is a non-parametric metric utilized in RKHS to gauge the anticipated resemblance of two spreads. That is articulated as formula (11):

$$MMD(X_s, X_t) = ||E_{x_i^s \sim D_s}[\varphi(F(x_i^s))] - E_{x_j^t \sim D_s}[\varphi(F(x_j^t))]||_\Omega^2 \quad (11)$$

Among these, φ(·) denotes the non-linear correspondence operation, and Ω denotes that such separation is realized by inserting the extracted attributes As measured in RKHS, E(·) denotes the statistical anticipation. DANN can be utilized to forecast categorical signals. Nevertheless, the attribute selector trained by DANN creates a challenge for the field differentiator to identify the discrepancy among the two fields, so GAM-MTN requires to handle three aspects after the diagram is produced: attribute selector (F), label predictor (C) and field differentiator Component (D). In order to acquire transferable attributes and simulate the aforementioned three categories of attribute details, the comprehensive goal operation is arranged as a mixture of categorization cost, field adjustment cost, and structure adjustment cost.

Utilize cross-entropy cost to estimate the actual and forecasted tags. The categorization cost is computed as $L_C(X_s, Y_s) = E_{(x_i^s, y_i^s) \sim D_s} L(C(x_i^s), y_i^s)$ where $C(x_i^s)$ signifies the prediction outcome of the class predictor and $L(\cdot,\cdot)$signifies the cross-entropy cost.

To tackle the field covariate shift, a field differentiator is utilized to retrieve attributes from the origin and destination fields, and an attribute extractor is trained to deceive the field differentiator. The field adjustment cost is determined as formula (12):

$$L_{DA}(X_s.X_t) = E_{x_i^s \sim D_s}[log(1-D(F(x_i^s)))] + E_{x_i^t} - D_t\left[log(D(F(x_j^t)))\right] \quad (12)$$

where $F(x_i^s)$ and $F(x_j^t)$ signify the retrieved attributes of the i-th origin instance and the j-th destination instance individually. The $D()$figure is 0 or 1, which is utilized to differentiate which field the instance pertains to.

Utilize MMD to match the attribute frameworks of the origin and destination fields. The framework alignment cost is determined as formula (13):

$$L_{MMD}(X_s, X_t) = ||E_{x_i^s \sim D_s}[\varphi(F(x_i^s))] - E_{x_j^t \sim D_s}[\varphi(F(x_j^t))]||_\Omega^2 \quad (13)$$

The comprehensive goal operation to realize unsupervised field adjustment can be articulated as formula (14):

$$L_{Total}(X_s, Y_s, X_t) = L_c(X_s, Y_s) + rL_{DA}(X_s, X_t) + kL_{MMD}(X_s, X_t) \quad (14)$$

## 3. EXPERIMENTAL ANALYSIS

### 3.1 MEMS photoacoustic pool design

Appropriate photoacoustic pool geometry is beneficial to the enhancement of photoacoustic signals and the improvement of system sensitivity. Therefore, it is particularly important to find the optimal size of the photoacoustic pool. This article uses limited segment application simulation to find the optimal size of the photoacoustic pool, and conducts experimental verification based on the simulation results.

The gas concentration is controlled to 5000 ppm and the frequency is 7 Hz. The parameter values of the extent, breadth and elevation of the photoacoustic cavity are changed in sequence, and the model is parametrically scanned to obtain the influence of the extent, breadth and elevation of the photoacoustic cavity on the sound pressure signal. The emulation outcomes are displayed in Figures 6,7.

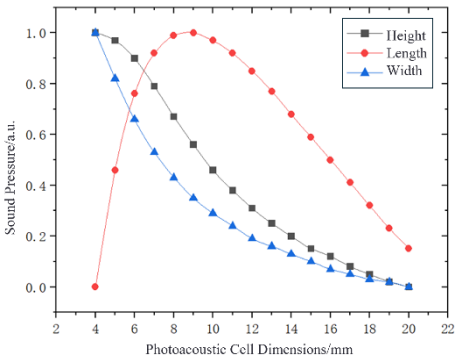


Fig. 6. Acoustic Pressure Signal from Light Source

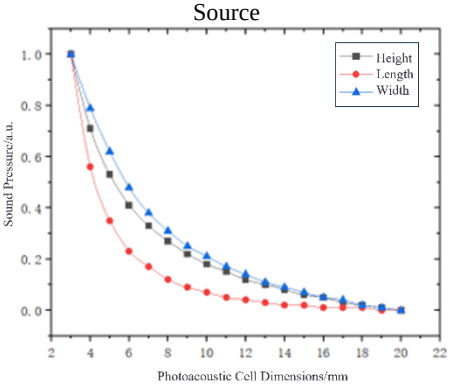


Fig. 7. Acoustic Pressure Signal from Heat Source

It may be observed from Image 6 that the rise in the length and width of the photoacoustic cavity will cause the sound pressure signal of the light source to weaken. However, when the height of the photoacoustic cavity increases, the sound pressure of the light source exhibits a pattern of initially rising and subsequently falling, and attains 9 mm. peak. Rising in the length, width and height of the photoacoustic cavity raises volume of the photoacoustic cavity, which will lead to the weakening of the acoustic pressure indication of the illumination origin. However, the increase in the height of the photoacoustic cavity is also accompanied by the lengthening of the light route. When the optical path becomes longer, the absorbed light energy increases, the number of excited molecules increases, and the excited sound pressure signal also increases. Therefore, under the combined action of these two factors, the sound pressure of the light source will first increase and then decrease as the height of the photoacoustic cavity increases. It may be observed from Image 7 that extent the length, width, and height of the photoacoustic cavity will weaken acoustic stress indication of the thermal origin. The acoustic stress signal of the heat source is not affected by the length of the optical path like acoustic stress indication of the light source. Therefore, the heat energy released by the heat source remains unchanged. The increase in the length, width, and height of the photoacoustic cavity causes the volume of the photoacoustic cavity to increase, and acoustic stress indication of heat source in the cavity decreases.

From the perspective of light source sound pressure signal detection, the optimal height of the photoacoustic cavity is 9 mm, and the shorter the length and width of the photoacoustic cavity, the better. For a specific photoacoustic cavity, the light source sound pressure signal exists in the form of a sine wave, and its frequency is consistent with the adjustment frequency of the MEMS infrared illumination origin. Affected by the heat generated by the MEMS infrared light source, in addition to the light source sound pressure signal, there is also a heat source in the photoacoustic cavity. For the sound pressure signal, the latter is much larger than the former and exists as a constant value.

Since the actual size of the photoacoustic cavity is limited by the technology level, the size of the MEMS infrared light source and the MEMS microphone, the optimal length, width, and height of the photoacoustic cavity are determined to be 7 mm, 5 mm, and 9 mm respectively.

### 3.2. GAM-MTN model verification analysis

To illustrate the superiority of the GAM-MTN model, experiments were conducted, and all migration tasks are defined as source domain target domain. The transformer parameter data collected by MEMS photoacoustic sensors under four working conditions (D1-D4) were selected. In the experiment, the transformer was in various states, including normal (N), partial discharge (PD), low energy discharge (F1), high energy discharge (F2), medium and low temperature overheating (T1) and high temperature overheating (T2). Each failure mode contains 204,800 data points, that are arranged in 100 instances; every instance includes 2,048 data entries. The design transfer tasks are D1-D2, D1-D3, D1-D4, D2-D3, D2-D4, and D3-D4. Transferring tasks D1-D2 indicates that the framework is educated on the tagged origin data collection gathered in operational situation D1 and shifted to the untagged destination data collection gathered in operational situation D2. In the dataset, each sample consists of 2048 data points containing sufficient fault information, and the number of samples obtained under each fault is 1000. The data collection is partitioned into training collection and testing collection based on the proportion of 6:4.

During education, the number of iterations is set to 900. Considering that parameter settings have a significant impact on the framework diagnosis results, the numerical span of the penalty factor is {0.2, 0.4, 0.6, 0.8, 1}, and the numerical span of the amount of mappings is {1, 2, 3, 4, 5}, as shown in Figure 8, depicts the impact of the penalty parameter and the number of mappings on the framework fault diagnosis precision. It may be observed that when the penalty parameter is assigned to 0.6 and the quantity of mappings is assigned to 3, the model reaches the peak on the data set. Best accuracy performance. Therefore, this set of parameter configurations was selected.

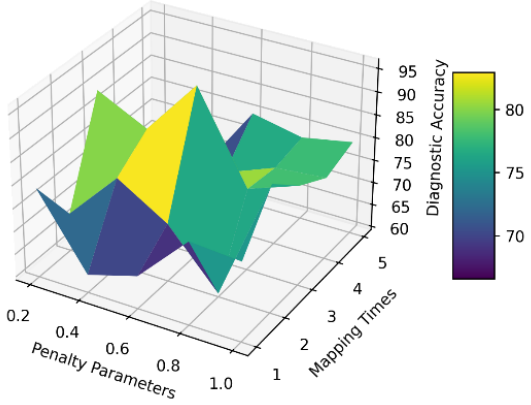


Fig. 8. The relationship between penalty parameters, mapping times, and diagnostic accuracy

To confirm the efficiency of the framework, compare it with the performance of the following neural network: MK-MMD (Multiple Kernel Maximum Mean Discrepancy) is a method that uses multiple kernel functions to assess the spread discrepancy among the origin field and the destination field, which can effectively capture the differences between different feature spaces are suitable for many types of data. The calculation is relatively simple and easy to implement. CORAL (Correlation Alignment) is a method to achieve feature alignment by reducing the discrepancy

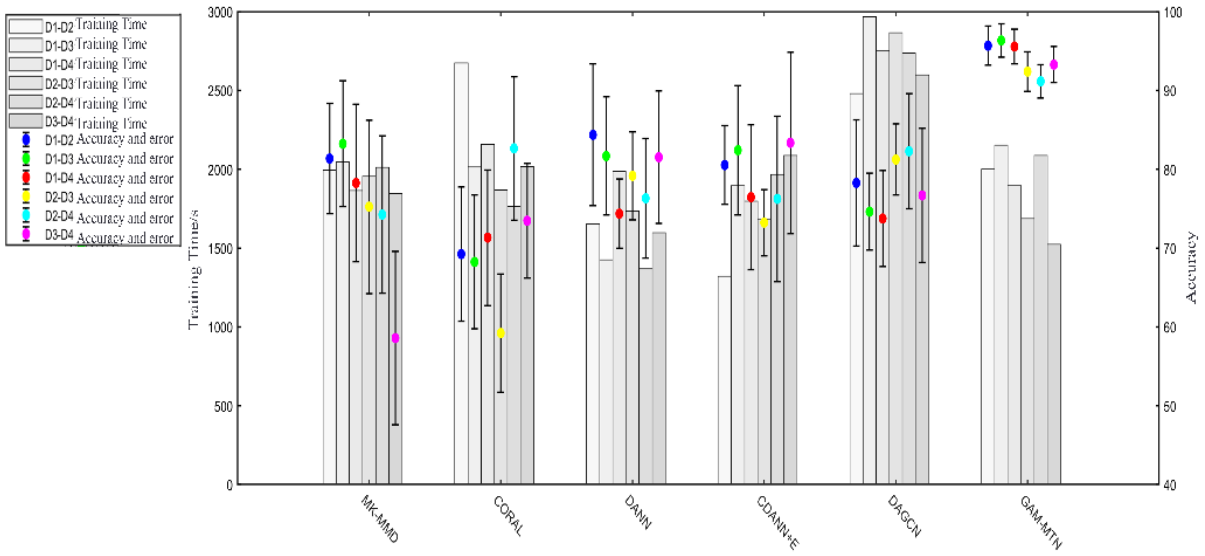


Fig. 9. Comparison of Diagnosis Accuracy and Training Time for Different Networks

among the secondary statistical moments (covariance matrices) of the origin field and the destination field. It has high computational efficiency, is suitable for large-scale data sets, and is simple to implement, easy to integrate into existing deep learning frameworks. DANN (Domain-Adversarial Neural Networks) is a method that allows the attribute extractor to acquire field-invariant attributes by introducing a domain discriminator. It can effectively handle the field shift issue. The model structure is clear and the theoretical foundation is solid. It is suitable for many applications. An unsupervised domain adaptation task. CDANN+E (Conditional Domain-Adversarial Neural Networks with Entropy Minimization) is a method that adds conditional domain adversarial and entropy minimization modules based on DANN. It can better handle the category disparity issue and enhance the categorization efficiency of the framework. Through entropy Minimization further enhances the discriminability of features and improves the robustness of the model. DAGCN (Dual Attention Graph Convolutional Network) is a method that combines graph convolutional networks and dual attention mechanisms. It can effectively process non-Euclidean spatial data and extract complex features in graph structures. Through the dual attention mechanism, it improves Feature representation ability and model interpretability.

Figure 9 shows the training time, training accuracy and error corresponding to each neural network model under each task. Figure 10 shows the average training accuracy of each network under each task.

Experimental results show that GAM-MTN exhibits significant advantages in diagnostic accuracy. GAM-MTN can provide higher accuracy when handling fault diagnosis tasks of dissolved gases in transformer oil under complex working conditions. Regardless of the working conditions,

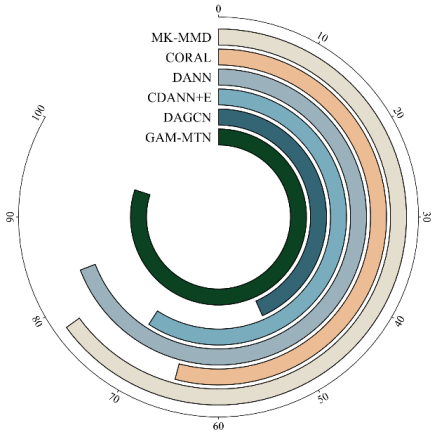


Fig. 10. Average Training Accuracy for Different Networks on Various Task

the diagnostic accuracy of GAM-MTN is significantly higher than other models. This is due to GAM-MTN's unique sample mapping method, which makes the sample distribution in the origin field and the destination field more even, thus improving the overall migration effect. This sample distribution optimization not only helps reduce inter-domain differences, but also achieves better adaptability at the feature level, ensuring the consistency and stability of the framework in various operational situations. Secondly, the data of dissolved gases in transformer oil often have complex structures and nonlinear relationships. GAM-MTN adds a measure of node similarity to change the processing of aggregation weights and performs well in processing non-Euclidean space data, can effectively handle this type of data. This capability improves the precision of feature extraction, and significantly increases the convergence velocity of the framework. In contrast, other models such as MK-MMD, CORAL, DANN and CDANN+E cannot efficiently process non-Euclidean geometric attributes, resulting in low diagnostic accuracy under complex working

conditions. Although DAGCN has made improvements in processing non-Euclidean spatial data, its internal convolutional neural network (CNN) makes the running time longer, affecting the efficiency in practical applications. GMMTN performs well in processing non-linear geometric information, and further improves the model's convergence speed and reduces running time by optimizing the sample mapping method.

In order to study and understand the classification ability of the model in each category, the confusion matrix of each model as shown in Figure 11 was made based on experiments.

The confusion matrix displays the diagnostic precision of each framework in various fault categories. It may be observed that GAM-MTN performs well in the diagnosis of most fault categories, especially in the diagnosis of PD and F1 faults, achieving high accuracy. In contrast, other

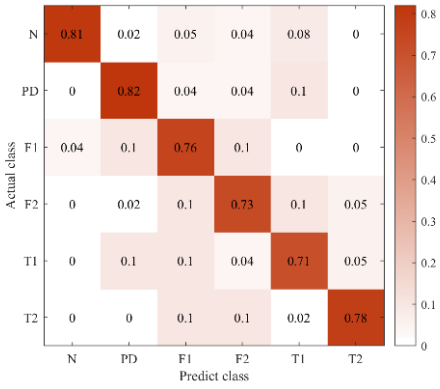


(a) Confusion Matrices for MK-MMD

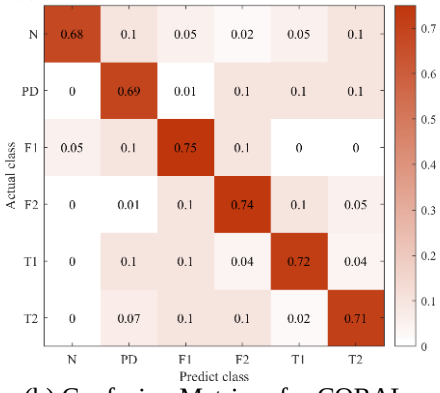


(b) Confusion Matrices for CORAL

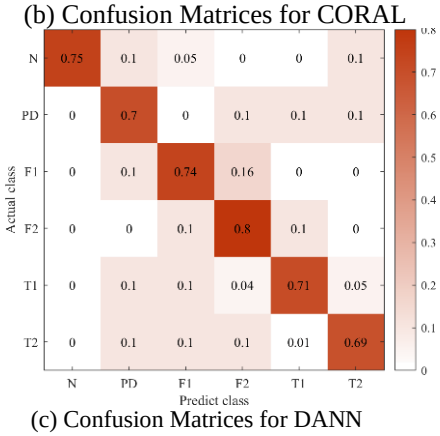


(c) Confusion Matrices for DANN

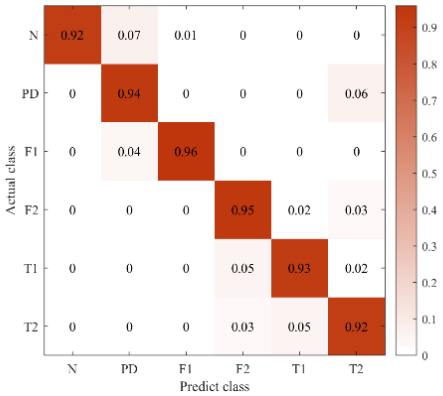


(d) Confusion Matrices for CDANN+E

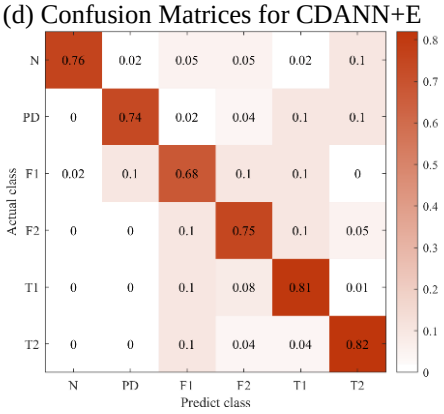


(e) Confusion Matrices for DAGCN

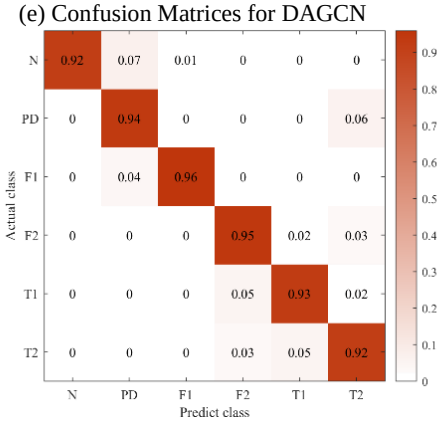


(f) Confusion Matrices for GAM-MTN

Fig. 11. Confusion Matrices for Different Networks

models perform poorly in diagnosing certain fault categories. For example, MK-MMD made many errors in diagnosing PD type faults, while CORAL performed poorly in diagnosing F2 type faults. This suggests that these models may be inadequate in handling certain types of failures. GAM-MTN significantly improves its diagnostic accuracy and stability under complex working conditions by optimizing sample distribution and adding a measure of node similarity to change the processing of aggregation weights.

In Figure 12, through the visualization results of the t-SNE graph, we can clearly see the superiority of GAM-MTN in processing origin field and the destination field data. GAM-MTN can cluster the data in the origin field and the destination field into 6 clear centers respectively. The data points of each category form obvious clustering areas, showing

excellent feature extraction and category retention capabilities. In contrast, other models MK-MMD and DAGCN have fuzzy clustering centers on some data points of most categories, and the distribution of data points is scattered, making it difficult to form clear category boundaries. In addition, GAM-MTN achieves better separation between data points of different categories with almost no cross-overlap, indicating its higher accuracy in classification tasks. These advantages make GAM-MTN notably superior to other frameworks in aspects of cross-domain adaptability and high-precision classification.

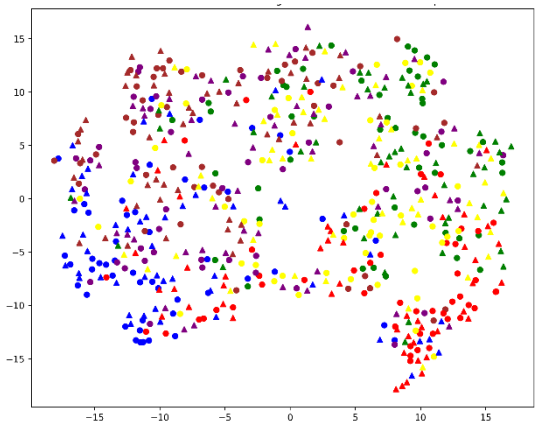

(a) t-SNE Plots for MK-MMD

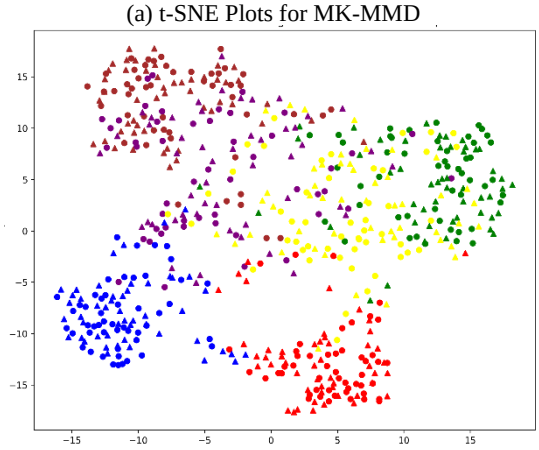

(b) t-SNE Plots for DAGCN

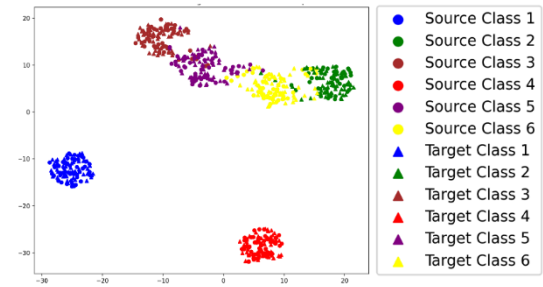


(c) t-SNE Plots for GAM-MTN

Fig. 12. t-SNE Plots for Different Models

## 4. CONCLUSIONS

This paper addresses the challenges of feature distribution shift and domain adaptation in cross-condition fault diagnosis of power transformers by proposing an innovative diagnostic framework based on graph-structured transfer learning. By constructing a dynamic graph convolutional network and a cross-domain mapping co-optimization mechanism, the framework achieves efficient feature decoupling and knowledge transfer from multi-source heterogeneous monitoring data. This method overcomes the reliance of traditional diagnostic models on the completeness of labeled data, leveraging the topological modeling advantages of graph neural networks to effectively capture the nonlinear relationships between fault characteristics and operational condition interference factors. Additionally, through a hierarchical domain adaptation strategy, it accomplishes stable transfer from laboratory-calibrated data to complex field environments under unsupervised conditions. Theoretical analysis and engineering validation demonstrate that the framework significantly enhances the distinguishability of fault patterns in cross-domain scenarios and the generalization capability of the diagnostic system. The research findings provide universal reference value for the intelligent diagnosis of critical power equipment such as transformers. Future work will focus on exploring multi-physical field information fusion and lightweight deployment solutions for edge computing, promoting the large-scale application of this method in fault early warning for new power systems.

**Source of funding:** *This research was funded by the Science and Technology Project of State Grid Qinghai Electric Power Company (522802240006).*

**Author contributions:** *research concept and design, B.F.; Collection and/or assembly of data, S.L.; Data analysis and interpretation, J.L.; Writing the article, J.P.; Critical revision of the article, X.Z.; Final approval of the article, S.M.*

**Declaration of competing interest:** *The authors declare that they have no known competing financial interests or personal relationships that could have appeared to influence the work reported in this paper.*

## REFERENCES

1. Shao YY, Wang X, Peng P, et al. Intelligent diagnosis method for dry transformer condition based on machine vision and auditory response. Noise and Vibration Control. 2024;44(04):199-204.
2. Sun T, Chen X, Du MS, et al. Transformer fault diagnosis method based on DGA using Light GBM-ICOA-CN. Proceedings of the CSEE, 1-10.
3. Yang X, Zhou W, Cheng L, et al. Research on fault diagnosis of transformers based on multi-source information fusion using KPCA-SVM. 2024 4th International Conference on New Energy and Power Engineering (ICNEPE). 2025. https://doi.org/10.1109/ICNEPE64067.2024.10860520
4. Wang FR, Li Z. Transformer fault diagnosis model based on SCSSA-BiLSTM. Southern Power System Technology. 2024:1-9.

5. Wen J, Yuan J, Zheng Q, et al. Hierarchical domain adaptation with local feature patterns. Pattern Recognit. 2022;124:108445. https://doi.org/10.1016/j.patcog.2021.108445.
6. Hu T, Guo Y, Gu L, et al. Remaining useful life prediction of bearings under different working conditions using a deep feature disentanglement based transfer learning method. Reliab. Eng. Syst. Saf. 2022; 219:108265. https://doi.org/10.1016/j.ress.2021.108265.
7. Li T. Wavelet Kernel Net: An interpretable deep neural network for industrial intelligent diagnosis. IEEE Trans. Syst., Man, Cybern., Syst. 2022;52(4): 2302–2312. https://doi.org/10.1109/TSMC.2020.3048950
8. Wang D, Chen Y, Shen C, Zhong J, Peng Z, and Li C. Fully interpretable neural network for locating resonance frequency bands for machine condition monitoring. Mech. Syst. Signal. Process. 2022;168: 108673. https://doi.org/10.1016/j.ymssp.2021.108673.
9. Ganin Y. Domain-adversarial training of neural networks. J. Mach. Learn. Res. 2016;17(1):2096–2030.
10. Zhao D, Zhang H, Liu S, Wei Y, and Xiao S. Deep rational attention network with threshold strategy embedded for mechanical fault diagnosis. IEEE Trans. Instrum. Meas. 2021;70:3519715. https://doi.org/10.1109/TIM.2021.3085951
11. Scarselli F, Gori M, Tsoi AC, et al. The graph neural net-work model J. IEEE Transactions on Neural Networks. 2008;20(1):61-80. https://doi.org/10.1109/TNN.2008.2005605
12. Li T, Zhao Z, Sun C, et al. Domain adversarial graph convolutional network for fault diagnosis under variable working conditions. IEEE Trans. Instrum. Meas. 2021;70:1–10. https://doi.org/10.1109/TIM.2021.3075016
13. Bruna J, Mallat S. Invariant scattering convolutionnet-works. IEEE Transactions on Pattern Analysis and Machine Intelligence. 2013;35(8):1872-1886. https://doi.org/10.1109/TPAMI.2012.230.
14. Defferrard M, Bresson X, Vandergheynst P. Convolutional neural networks on graphs with fast localized spectral filtering. Advances in Neural Information Processing Systems. 2016;29:3844-3852.
15. Pang S, Yang X, Zhang X, et al. Fault diagnosis of rotating machinery components with deep ELM ensemble induced by real-valued output-based diversity metric. Mech. Syst. Signal Process. 2021;159:107821. https://doi.org/10.1016/j.ymssp.2021.107821.
16. Goay CH, Ahmad NS, Goh P. Transient simulations of high-speed channels using CNN-LSTM with an adaptive successive halving algorithm for automated hyperparameter optimizations. IEEE Access. 2021;9: 127644–127663. https://doi.org/10.1109/ACCESS.2021.3112134.
17. Zhu J, Ju Y, Xia M. Vehicle recognition model based on improved CNN-SVM. in Proc. 2nd Int. Seminar Artif. Intell., Netw. Inf. Technol. 2021:294–297. https://doi.org/10.1109/AINIT54228.2021.00065.
18. Jin T, Yan C, Chen C, et al. Light neural network with fewer parameters based on CNN for fault diagnosis of rotating machinery. Measurement. 2021;181:109639. https://doi.org/10.1016/j.measurement.2021.109639.
19. Lavasani HM, Wanling P, Harrington B, et al. A 76 dB 1.7 GHz 0.18 µm CMOS tunable TIA using broadband current pre-amplifier for high frequency lateral MEMS oscillators. IEEE J. Solid-State Circuits. 2011;46:224-235. https://doi.org/10.1109/JSSC.2010.2085890.
20. Kamada Y, Isobe A, Oshima T, et al. Capacitive MEMS accelerometer with perforated and electrically separated mass structure for low noise and low power. J. Microelectromech. Syst. 2019;28(3):401-408. https://doi.org/10.1109/JMEMS.2019.2903349.
21. Akita I, Okazawa T, Kurui Y, et al. A feedforward noise reduction technique in capacitive MEMS accelerometer analog front-end for ultra-low-power IoT applications. IEEE J. Solid-State Circuits. 2020;55(6):1599-1609. https://doi.org/10.1109/JSSC.2019.2952837.

**Jiaqi PENG** received the Master's degree from the Lanzhou Jiaotong University. He is currently working in Haidong Power Supply Company of Qinghai Grid Corporation. His current research interests include high voltage and insulation technology and substation operations.
e-mail: pjq15597275739@163.com

**Baomin FANG** received the Bachelor's Degree from the North China Electric Power University. He is currently working in Haidong Power Supply Company of Qinghai Grid Corporation. His main research direct is substation relay protection.
e-mail: myl123007@sina.com

**Shou LI** received the Bachelor's Degree from the Xi'an University of Technology. He is currently working in Haidong Power Supply Company of Qinghai Grid Corporation. His main research direct is substation secondary technology.
e-mail: 124270163@qq.com

**Jin LUO** received the Bachelor's Degree from the Nanjing University of Science and Technology. He is currently working in Haidong Power Supply Company of Qinghai Grid Corporation. His main research direct is transmission and distribution operation inspection.
e-mail: 997154217@qq.com

**Xiaobin ZHU** received the Bachelor's Degree from the Zhengzhou University. He is currently working in Haidong Power Supply Company of Qinghai Grid Corporation. His main research direct is substation maintenance.
e-mail: 543261426@qq.com

**Shunqing MA** received the Bachelor's Degree from the Qinghai University. He is currently working in Haidong Power Supply Company of Qinghai Grid Corporation. His main research direct is electrical test.
e-mail: 705704959@qq.com